RSC Advances

PAPER

View Article Online
View Journal | View Issue



Cite this: *RSC Adv.*, 2022, **12**, 32986

# Morphological and optical investigation of 2D material-based ternary nanocomposite: $Bi_2O_3$/MgO/GO synthesized by a co-precipitation technique

Ashwa Urooj,[a] Malika Rani, *[a] Aqeel Ahmad Shah,[b] Samina Aslam,[c] Rabia Siddiqui,[a] Aisha Siddiqa,[a] R. Neffati [de] and Ali Dad Chandio [b]

A ternary oxide nanocomposite based on $Bi_2O_3$/MgO/GO was prepared using a co-precipitation method for photoconductive device applications. The structure and morphology of the as-prepared nanocomposite were characterized analytically using X-ray diffraction (XRD), scanning electron microscopy (SEM), electron dispersive spectroscopy (EDS) techniques, and optical characterization was made using Fourier-transform infrared (FTIR) spectroscopy, photoluminescence (PL), and UV-vis spectroscopy techniques. The heterostructure of the crystal with a crystallite size of 28.064 nm and the purity of the phase are depicted by XRD patterns. Scanning electron microscopy revealed its morphology showing an average grain size of 0.27 μm, and the purity of the nanocomposite was confirmed by EDS, which showed the presence of Mg, Bi, C, and O. The band gap of the $Bi_2O_3$/MgO/GO nanocomposite was 4.02 eV by PL comparable with 5.718 eV by UV-vis spectroscopy, which evidenced that the material may have potential applications in far UVC emissive devices. The zeta potential observed was 48.0 mV, indicating the stability of the ternary nanocomposite.

Received 29th July 2022
Accepted 11th October 2022

DOI: 10.1039/d2ra04760h

rsc.li/rsc-advances



## 1 Introduction

Since the last two decades, research on GO has been an emerging area for scientists because of its various fascinating properties. Graphene (single layer hexagonal lattice with $sp^2$-bonded carbon atoms) has unique properties.[1–5] After the pragmatic innovation of graphene sheets in 2004, research on graphene-based materials has intensified.[6] The identical large theoretically calculated surface area (2620 $m^2$ $g^{-1}$) with a possibly small manufacturing cost of graphene makes it an advantageous and encouraging material for its concrete applications in the management of environmental pollutants.[7,8] van der Waals interactions between the atoms of graphene make conservation of its enormous surface area challenging.[9] The removal of metals from water and gaseous pollutants in the atmosphere has been studied using modified graphite oxides.[10–22] Development in reducing the effects of aiming pollutants is achieved using amendment in carnal properties and apparent chemistry of graphite oxide. Presently, numerous GO-based metal/metal oxide composites are extensively used as capacitors and biosensors.[23–26] Bismuth oxide ($Bi_2O_3$) has been inspected comprehensively owing to its electrical and optical properties such as photoconductivity, photoluminescence, dielectric permittivity, refractive index, and large energy band gap. All these properties make bismuth oxide a potential candidate for its uses in areas including optoelectronic devices and sensors.[27,28] However, alkaline earth metal like magnesium oxide (MgO) show its properties like simplicity of association with other elements of composite and pronounced adsorption capacity.[29,30] Also, MgO nanoparticles (MgO NPs) have been used for the removal of formaldehyde, catechol, dyes, phenol, and fluoride from wastewater.[29–34] Hence, for the removal of pollutants, GO decorated with MgO NPs, *i.e.* GO/MgO nanocomposites (NCs) can be revealed as potential adsorbents. The enormous band gap of MgO (≈5 eV) is a limiting factor for its oxidative uses. Thus, employing ZnO (band gap ≈ 3.2 eV) as a pairing agent with MgO realizes the narrowing of the band gap in a nanocomposite, improving the active sites. The reduced light adsorption in semiconductors, nanoparticle size, and their pronounced affinity to agglomerate, which declines the active surface area of the catalyst, is an issue that needs to be considered.[35,36]

[a]*Wet Chemistry Laboratory, Department of Metallurgical Engineering, NED University of Engineering and Technology, Karachi, 75270, Pakistan. E-mail: dr.malikarani@yahoo.com*

[b]*Department of Metallurgical Engineering, NED University of Engineering and Technology, 75270, Karachi, Pakistan*

[c]*Department of Chemistry, The Women University Multan, 66000, Pakistan*

[d]*Department of Physics, King Khalid University, P. O. Box 9032, Abha 61413, Kingdom of Saudi Arabia*

[e]*Laboratoire de Physique de la Matière Condensée, Département de Physique, Faculté des Sciences de Tunis, Université Tunis El Manar, Campus Universitaire, 1060 Tunis, Tunisia*

Oxides of bismuth (Bi) are perceived as very potent *in lieu* of the dynamic visible light, particularly the hybridization of O 2p and Bi 6s states, primarily in the formation of a tapered band gap; this is why the photocatalytic reaction of ZnO has been enhanced.[37–39] A heterostructure based on Bi-oxide, *i.e.*, $Bi_2O_3$–ZnO[40] shows its coupling to enhance the photo-catalytic activity, which decelerates the proportion of $Bi_2O_3$, in recombination of the photo-induced electron–hole pairs. Owing to the tapered band gap of 2.8 eV, $Bi_2O_3$ is a promising candidate for photo-catalytic activity because of its capacity to corrode $H_2O$.[41–44]

Owing to the properties of $Bi_2O_3$, MgO, and GO it was decided to study the nanocomposite's behavior using these oxides, which may change its band gap, so that it can be used for other applications such as photovoltaic energy storage and in far UVC emissive devices.

The $Bi_2O_3$/MgO/GO family has nevertheless been investigated to the best of our knowledge. In the current study, we investigated the $Bi_2O_3$/MgO/GO nanocomposite prepared *via* a co-precipitation method. The prepared sample ($Bi_2O_3$/MgO/GO) was studied and investigated and it exhibited a large energy gap in the UV-vis analysis. Results unveil a pronounced efficiency for photovoltaic and far UVC emissive devices in future applications. Their characteristics were studied using X-ray diffraction (XRD), FTIR spectroscopy, scanning electron microscopy (SEM), energy dispersive electron spectroscopy (EDX), Raman spectroscopy, photoluminescence (PL), UV-vis analysis, and zeta potential analysis. The main objective of the present research is to study the changes in the energy gap regarding the suitability of this composite for various applications in the treatment of UV-visible light.

## 2 Experimental section

### 2.1. Materials and preparation

**2.1.1. Chemicals.** Graphite powder, potassium permanganate ($KMnO_4$), sodium nitrate ($NaNO_3$), hydrochloric acid (HCl), sulphuric acid ($H_2SO_4$), distilled water, magnesium(II) nitrate hexahydrate [$Ni(NO_3)_2 \cdot 6H_2O$], bismuth(III) nitrate pentahydrate [$Bi(NO_3)_3 \cdot 5H_2O$], sodium hydroxide (NaOH), and ethanol were all purchased from Sigma-Aldrich and used without verification.

**2.1.2. Preparation of graphene oxide.** Graphene oxide was prepared by Hummers technique *via* the oxidation of graphite.[45–47] Step-wise Hummers' method that we used is as follows:

• Graphite powder (2 g) and sodium nitrate ($NaNO_3$) (2 g) were dissolved in 50 mL of sulphuric acid ($H_2SO_4$) in a 1000 mL beaker with constant stirring on an ice bath (0–5 °C).

• The temperature of the solution was maintained for 2 h. Then, potassium permanganate (6 g) was gradually and slowly added to the solution for maintaining its temperature below 15 °C.

• Then, 184 mL of distilled water was gradually poured and the solution was stirred for 2 h. After removing the ice bath, the suspension was stirred for 2 h at 35 °C.

• For 10–15 min the above solution was maintained in a reflux system at 98 °C. It changed the temperature to 30 °C and after 10 min it gave a brown-colored solution.

• After 10 min the temperature was decreased to 25 °C and maintained for 3 h.

• Finally, 40 mL of hydrogen peroxide ($H_2O_2$) was added to the reaction mixture, which lightened up the dark colour of the solution to bright yellow.

• A 200 mL of water was added to the above solution and stirred for 1 h.

• Stirring was stopped and the solution was placed at room temperature. After 3–4 h, the particles settled down to the bottom of beaker and the residual water is poured to filtration process.

• The resultant solution was centrifuged several times adding 10% HCl and DI water until it formed a gel-like texture and the pH became neutral.

• The gel-like material was vacuum dried at 60 °C for more than 24 h to obtain graphene oxide (GO) granules for our nanocomposite.

**2.1.3. Preparation of $Bi_2O_3$/MgO/GO ternary nanocomposite by the co-precipitation method.** The following steps for the co-precipitation method[48–52] were used in the preparation of $Bi_2O_3$/MgO/GO ternary nanocomposite:

• 0.01 g of GO prepared by Hummers' method was dissolved in 100 mL of DI water in a beaker, which was sonicated for 60 min.

• Two solutions having 0.1 M of $Bi(NO_3)_3 \cdot 5H_2O$ and $Ni(NO_3)_2 \cdot 6H_2O$ each prepared individually were mixed with a solution of GO.

• The reaction bath obtained was placed on a hot plate for magnetic stirring at 70 °C. After maintaining the temperature at 70 °C, 0.1 M solution of sodium hydroxide was added to this solution to get neutral pH.

• For 1 h the solution was continuously stirred and heated at the same temperature. A black-colored precipitate was formed. The precipitate was washed three times with a solution of ethanol and distilled water before being dried in an oven at 50 °C.

• The nanocomposite attained was later annealed at a temperature of 150 °C for 2 h.

### 2.2. Characterizations

To determine the crystal phase and configuration of synthesized samples, a Bruker X-ray diffraction D8-Discover instrument was used with monochromatic high-intensity Cu-Kα radiation ($\lambda$ = 1.5406 Å). The surface state and structures of the prepared sample were observed using the JS M-6380A SEM (JEOL, Japan) instrument for SEM and EDX analysis. A PE Lamada 356 UV-vis spectrometer was used for UV-vis scanning spectrophotometry. A photoluminescent spectrometer (FLS1000 by Edinburgh Instruments) was used for PL analysis. The NanoBrook ZetaPlus analyser was used for zeta potential measurements. A Bruker FTIR spectrometer was used for the FTIR analysis.

## 3 Results and discussion

### 3.1. X-ray diffraction analysis

X-Ray diffraction is used to determine the phase and crystal structure of a material (Fig. 1).[53]

The XRD pattern of $Bi_2O_3$/MgO/GO with peaks at $2\theta$ values of 31°, 38°, 44°, and 64° represent (006), (113), (024), and (003) planes using the JCPDS card #76-1730 and 78-0430, indicating the peaks for $Bi_2O_3$ and MgO, respectively. A hump from 10° to 40° confirms the ternary nanocomposite formation. The area of crystalline peak is 838.425 $(au)^2$ and the area of all peaks is 957.312 $(au)^2$. The material crystallinity is observed using the formula in eqn (1).

$$\text{Crystallinity} = \frac{\text{area of crystalline peak}}{\text{area of all peak}} \times 100 \quad (1)$$

The crystallinity observed is 87% and the highest peak obtained is at 44° with the (024) plane. The advantage of this method is that all the functional groups are removed resulting in a favorable suppression of graphene onto the synthesized nanocomposite.[54] A strong diffraction peak centered at $2\theta = 10.3°$ with (001) peak of GO[55] having a crystallite size of 0.23 nm is elaborated in Table 1. The crystal size of GO significantly decreases in the nanocomposite. The FWHW of plane (024) is 0.295200 and thus the average crystallite size obtained through the Scherrer eqn (2) is 28.064 nm (Table 1).

$$D = \frac{K\lambda}{\beta \cos\theta} \quad (2)$$

### 3.2. Scanning electron microscopy (SEM)

The surface morphology of $Bi_2O_3$/MgO/GO was inspected using scanning electron microscopy. The nanocomposite of bismuth oxide and magnesium oxide are distributed over the surface of GO (Fig. 2). The SEM image shows the spherical particles of MgO with a fuzz-like structure distributed over GO in abundance, having a particle size of 0.4 μm.[56] Fig. 2 shows a prismatic plate-like structure of $Bi_2O_3$, approximately 15 mm in average, indicating that recrystallization has occurred at some

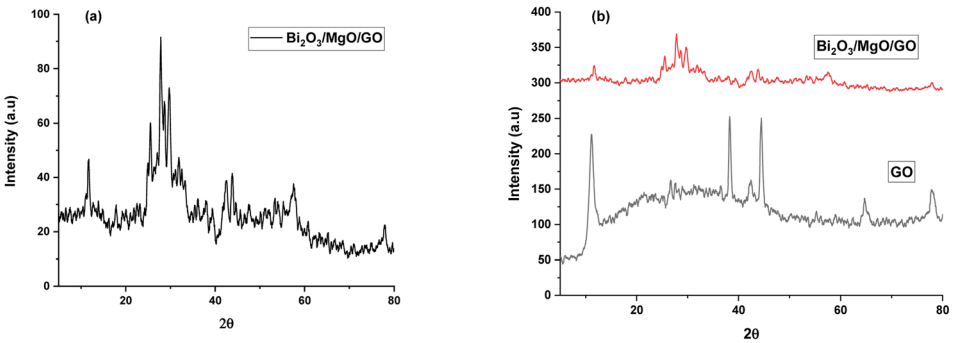


Fig. 1 XRD pattern of (a) $Bi_2O_3$/MgO/GO and (b) stacked XRD pattern of the ternary nanocomposite with GO.

Table 1 Parameters observed from the X-ray diffraction of $Bi_2O_3$/MgO/GO

| $2\theta$ (degree) | $\theta$ (degree) | Intense peak of FWHM | Miller indices | Crystalline size $D$ (nm) | (Average) $D$ (nm) |
|---|---|---|---|---|---|
| 11.13 (GO) | 5.56 | 0.63617 | 001 | 0.23 (GO) | 28.064 |
| 31.19 | 15.59 | 0.09662 | 006 | 85.36 | |
| 38.18 | 19.09 | 0.76094 | 113 | 11.04 | |
| 44.30 | 22.15 | 0.43316 | 024 | 19.80 | |
| 64.75 | 32.37 | 0.39360 | 003 | 23.89 | |

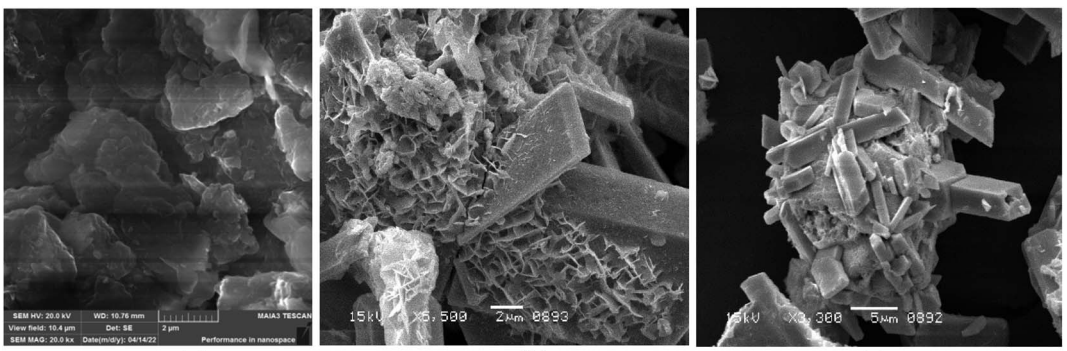


Fig. 2 SEM image of (a) GO and (b and c) $Bi_2O_3$/MgO/GO.

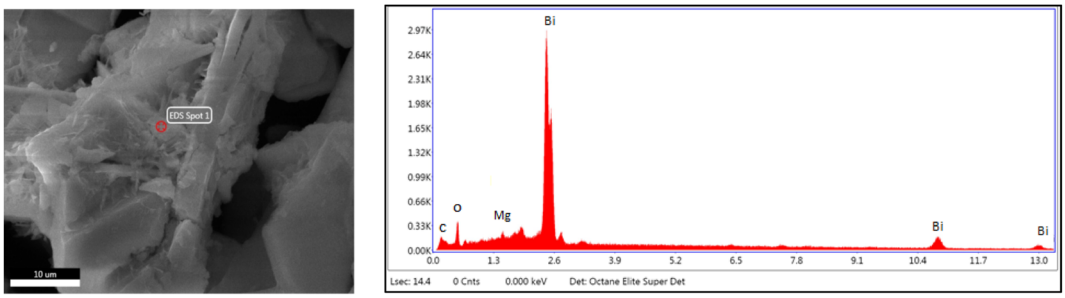


Fig. 3 Energy dispersive spectrum of the $Bi_2O_3$/MgO/GO nanocomposite.

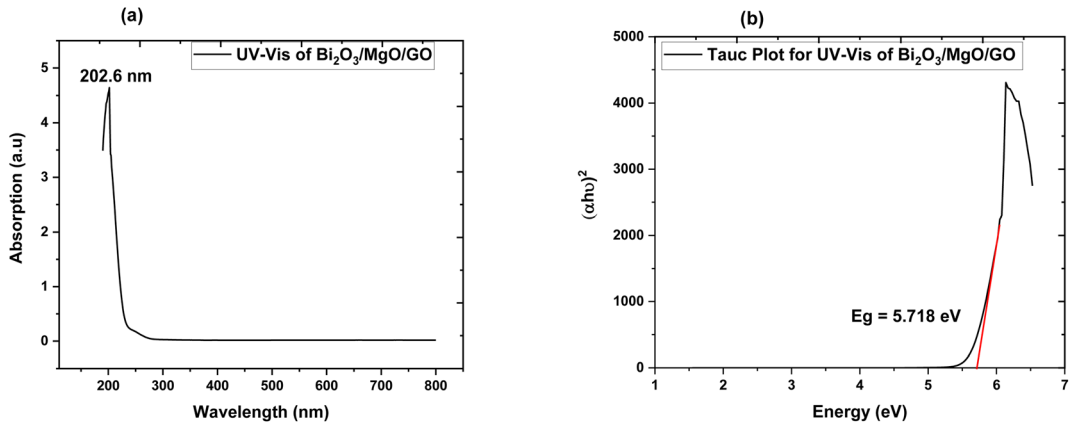


Fig. 4 (a) Absorption spectrum of $Bi_2O_3$/MgO/GO and (b) Tauc plot of $Bi_2O_3$/MgO/GO for direct band gap energy.

NaOH concentration, which improved its crystallinity.[57] The nanocomposite has an average grain size of 0.27 μm.

### 3.3. Energy dispersive spectroscopy (EDX)

The EDX method is used for determining the elemental composition or chemical analysis of a material. It is based on the interaction of samples with an X-ray source. Moseley's law precisely identifies the locations of peaks and is far superior than the EDX technique. The EDX of the ternary oxide nanocomposite, $Bi_2O_3$/MgO/GO, is shown in Fig. 3. The peak of carbon shows the presence of GO in the formation of the nanocomposite of $Bi_2O_3$ and MgO. The ratios of C, O, Mg, and Bi according to their atomic% and weight% are given in Table 2. A histogram is also shown along with Table 2 for a pictorial explanation of elements present in the composite. EDS is principally accurate up to the morsel quantity of metals present in the base material. It can be clearly seen from the graph that the percentage of bismuth is high in the heterostructure crystal of the $Bi_2O_3$/MgO/GO nanocomposite. The carbon peak is very small and its appearance indicates the presence of some species

Table 2 EDS results of the $Bi_2O_3$/MgO/GO nanocomposite

| Element | Weight% | Atomic% |
|---|---|---|
| C K | 13.21 | 21.23 |
| O K | 10.90 | 57.83 |
| Mg L | 20.62 | 8.3 |
| Bi M | 55.24 | 12.62 |

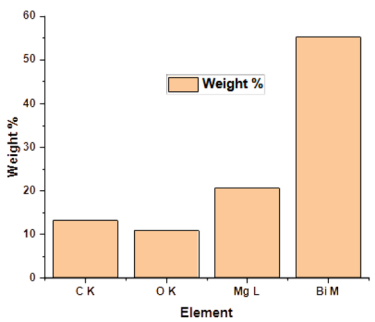

with carbon. As we are using GO, the probable reason for the appearance of the carbon peak in EDX is the presence of GO in the composite.

### 3.4. UV-vis spectroscopy

The band gap of ternary nanocomposite is measured *via* UV-vis spectroscopy. The modification in the optical band gap and the absorption behavior of films played an important role in opto-electronic device implementation.[58] The absorption spectrum obtained *via* UV-vis spectroscopy exhibits maximum absorption at 202.6 nm. The energy band gap value of the ternary nanocomposite measured using the Tauc plot is a direct band gap of 5.718 eV. This indicates the choice of the ternary nanocomposite as a favourable element for far UVC emissive device applications.

### 3.5. Zeta potential

Zeta potential is basically the measurement of the nanoparticle surface tension. A higher absolute value means a stronger repulsive force between the nanoparticles and a lower nanoparticle surface tension. Zeta potential is basically the measurement of particles that are dispersed and migrate with a potential difference.[59] The measurement of zeta potential are used to evaluate to surface electric potential such as electrophoresis, ultrasonic method and streaming potential to measure its stability.[60]

The changes during dilution are very sensitive. Consequently, the diluted solution measurement cannot determine the exact value of zeta potential.[61] The zeta potential is calculated by using Henry equation that is given by eqn (3),

$$\zeta = \frac{4\pi\eta}{\varepsilon} \times U \times 300 \times 300 \times 1000 \quad (3)$$

where $\varepsilon$ is the dielectric constant, $U$ is the mobility of electrophoretic, and $\eta$ is the viscosity of the solution. The zeta potential observed is 48.0 mV as shown in Fig. 5. The zeta deviation is 5.91 mV. The conductivity observed from the zeta potential graph is 0.0657 mS cm$^{-1}$. The value of conductivity for ternary nanocomposite evidence the presence of a large energy gap as calculated in UV-vis.[62]

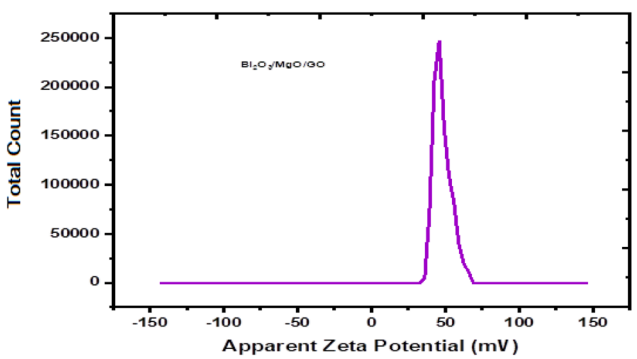


Fig. 5 Zeta distribution data of $Bi_2O_3$/MgO/GO.

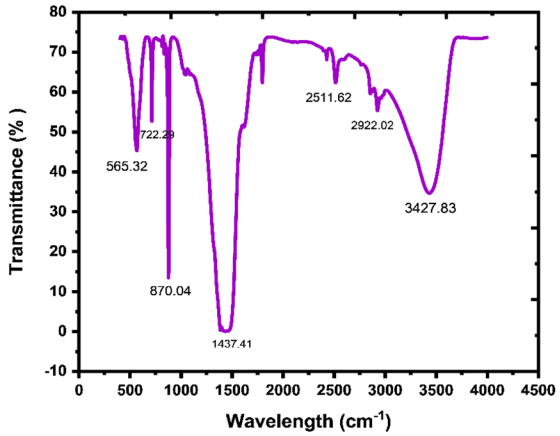


Fig. 6 FTIR spectra of $Bi_2O_3$/MgO/GO.

### 3.6. Fourier transform infrared (FTIR) spectroscopy

In the prepared material, the existence of bonding and functional groups can be analyzed using Fourier transform infrared spectroscopy. A study of FTIR is a crucial specification than any other absorption study and is used to represent an absorbent functional group.[63] In Fig. 6, there are peaks in the 565.32–722.29 cm$^{-1}$ region, which indicate vibrations in Mg–O and Bi–O bonds, and the peak at 870.04 cm$^{-1}$ indicates Bi–O–Bi bonding.[64] A broad band at around 1437.41 cm$^{-1}$ is because of the C=O stretching frequency, which exhibits the presence of an aromatic ring. Peaks at 2511.62 cm$^{-1}$ and 2922.02 cm$^{-1}$ show the existence of mono-saturated aromatic overtones. A broad band at around 3427.83 cm$^{-1}$ is attributed to the stretching frequency of H–O–H.[65] FTIR results show the existence of GO, $Bi_2O_3$, and MgO in the nanocomposite.

### 3.7. Photoluminescence

Photoluminescence is used to investigate the transfer behavior of photo-generated electrons and holes of semi-conductor substances. Photoluminescence causes an increase in quantum confinement by changing band gap.[66,67] Graphite with zero band gap does not exhibit photoluminescence properties but its band opens due to quantum confinement that comes due to a decrease in the size. Moreover, the band gap calculated is 4.02 eV using the formula in eqn (4), which is in close approximation to the calculated value of the UV-vis band gap energy *i.e.*, 5.718 eV. The difference in the band gap calculated using PL (Fig. 7) and UV-vis spectroscopy (Fig. 4) may be due to defects, impurities, dopants, and the contribution of the non-radiative energy transfer to the actual energy that is measured by the device.

$$E_g = \frac{1240}{\lambda(\text{nm})}(\text{eV}) \quad (4)$$

The band gap of GO calculated is in the 3.1–3.6 eV range and using FWHM it shows that the distribution of particles is in the nanometer scale.[68,69] The PL graph shows that the absorption peak moves towards a lower wavelength range in the ternary

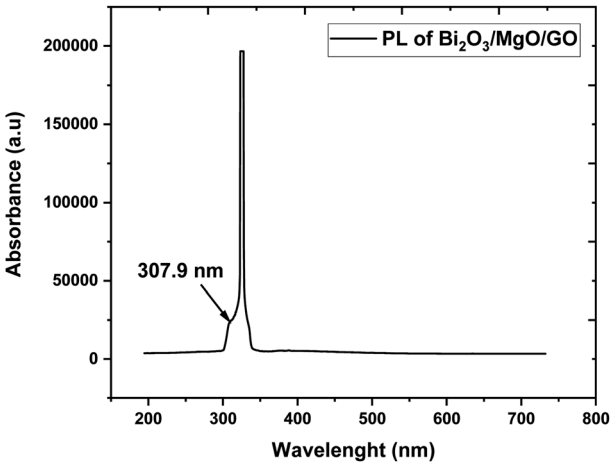


Fig. 7 Photoluminescence spectra of $Bi_2O_3$/MgO/GO.

nanocomposite and is in close approximation to the value of the energy gap calculated *via* UV-vis spectroscopy (Fig. 4).

## 4 Conclusion

$Bi_2O_3$/MgO/GO ternary oxide nanocomposite was prepared using the co-precipitation method. The nanocomposite obtained was characterized by SEM, XRD, EDS, UV-vis, PL, and FTIR techniques and using zeta potential. Crystallinity observed through X-ray diffraction is 87% and the average crystallite size is 35.02 nm. The band gap of the $Bi_2O_3$/MgO/GO nanocomposite obtained from PL spectroscopy is comparable with that obtained from UV-vis spectroscopy, which demonstrates its use in far UVC device applications. The value of zeta potential shows its excellent stability. In general, the characterizations of the 2D material-based ternary nanocomposite reveal its potential in photovoltaic and energy storage applications if it is further analyzed for its electrochemical and magnetic properties in future.

## Data availability

Data can be available on reasonable request.

## Author contributions

Ashwa Urooj: conceptualization, methodology, investigation, writing – original draft. Malika Rani: supervision, project administration, funding acquisition, resources. Aqeel Ahmad Shah: software, resources. Rabia Siddiqui: investigation, software, writing – review & editing, validation. Aisha Siddiqa: co-supervisor, revision and editing. Alidad Chandio: software, resources. Samina Aslam: writing – review & editing. R. Neffati: writing – review & editing, validation.

## Conflicts of interest

There is no conflict of interest.

## Acknowledgements

This work has been done under the supervision of Dr Malika Rani in the Department of Physics, The Women's University Multan. We are thankful for the Women University, Multan and the NRPU grant from the Higher Education Commission of Pakistan (HEC) that accommodates this project of Dr Malika Rani. The authors extend their appreciation to the Deanship of Scientific Research at King Khalid University for funding through Research Project under grant number R.G.P. 2/139/43.

## References

1 V. R. Posa, *et al.*, Graphene-ZnO nanocomposite for highly efficient photocatalytic degradation of methyl orange dye under solar light irradiation, *Korean J. Chem. Eng.*, 2016, **33**(2), 456–464.
2 K. S. Novoselov, *et al.*, Two-dimensional gas of massless Dirac fermions in graphene, *nature*, 2005, **438**(7065), 197–200.
3 J. C. Meyer, *et al.*, The structure of suspended graphene sheets, *Nature*, 2007, **446**(7131), 60–63.
4 M. Katsnelson and K. Novoselov, Graphene: new bridge between condensed matter physics and quantum electrodynamics, *Solid State Commun.*, 2007, **143**(1–2), 3–13.
5 F. Schedin, *et al.*, Detection of individual gas molecules adsorbed on graphene, *Nat. Mater.*, 2007, **6**(9), 652–655.
6 K. S. Novoselov, *et al.*, Electric field effect in atomically thin carbon films, *Science*, 2004, **306**(5696), 666–669.
7 G. Srinivas, *et al.*, Porous graphene oxide frameworks: synthesis and gas sorption properties, *J. Mater. Chem.*, 2011, **21**(30), 11323–11329.
8 M. Seredych, O. Mabayoje and T. J. Bandosz, Visible-light-enhanced interactions of hydrogen sulfide with composites of zinc (oxy) hydroxide with graphite oxide and graphene, *Langmuir*, 2012, **28**(2), 1337–1346.
9 M. Seredych, O. Mabayoje and T. J. Bandosz, Interactions of NO2 with zinc (hydr) oxide/graphene phase composites: visible light enhanced surface reactivity, *J. Phys. Chem. C*, 2012, **116**(3), 2527–2535.
10 M. J. Allen, V. C. Tung and R. B. Kaner, Honeycomb carbon: a review of graphene, *Chem. Rev.*, 2010, **110**(1), 132–145.
11 S.-T. Yang, *et al.*, Folding/aggregation of graphene oxide and its application in $Cu^{2+}$ removal, *J. Colloid Interface Sci.*, 2010, **351**(1), 122–127.
12 V. Chandra, *et al.*, Water-dispersible magnetite-reduced graphene oxide composites for arsenic removal, *ACS Nano*, 2010, **4**(7), 3979–3986.
13 V. Chandra and K. S. Kim, Highly selective adsorption of Hg 2+ by a polypyrrole–reduced graphene oxide composite, *Chem. Commun.*, 2011, **47**(13), 3942–3944.
14 C. Petit, M. Seredych and T. J. Bandosz, Revisiting the chemistry of graphite oxides and its effect on ammonia adsorption, *J. Mater. Chem.*, 2009, **19**(48), 9176–9185.
15 M. Seredych and T. J. Bandosz, Reactive adsorption of hydrogen sulfide on graphite oxide/Zr (OH) 4 composites, *Chem. Eng. J.*, 2011, **166**(3), 1032–1038.

16 M. Seredych and T. J. Bandosz, Effects of surface features on adsorption of SO2 on graphite oxide/Zr (OH) 4 composites, *J. Phys. Chem. C*, 2010, **114**(34), 14552–14560.
17 S. Bashkova and T. J. Bandosz, Adsorption/reduction of NO2 on graphite oxide/iron composites, *Ind. Eng. Chem. Res.*, 2009, **48**(24), 10884–10891.
18 Y. Matsuo, *et al.*, Removal of formaldehyde from gas phase by silylated graphite oxide containing amino groups, *Carbon*, 2008, **46**(8), 1162–1163.
19 K. Morishige and T. Hamada, Iron oxide pillared graphite, *Langmuir*, 2005, **21**(14), 6277–6281.
20 Y. Zhao, H. Ding and Q. Zhong, Preparation and characterization of aminated graphite oxide for CO2 capture, *Appl. Surf. Sci.*, 2012, **258**(10), 4301–4307.
21 B. Levasseur, C. Petit and T. J. Bandosz, Reactive adsorption of NO2 on copper-based metal−organic framework and graphite oxide/metal−organic framework composites, *ACS Appl. Mater. Interfaces*, 2010, **2**(12), 3606–3613.
22 C. Petit and T. J. Bandosz, Enhanced adsorption of ammonia on metal-organic framework/graphite oxide composites: analysis of surface interactions, *Adv. Funct. Mater.*, 2010, **20**(1), 111–118.
23 X. Zan, *et al.*, Freestanding graphene paper decorated with 2D-assembly of Au@ Pt nanoparticles as flexible biosensors to monitor live cell secretion of nitric oxide, *Biosens. Bioelectron.*, 2013, **49**, 71–78.
24 L. L. Zhang, *et al.*, Highly conductive and porous activated reduced graphene oxide films for high-power supercapacitors, *Nano Lett.*, 2012, **12**(4), 1806–1812.
25 M. Zhu, P. Chen and M. Liu, Graphene oxide enwrapped Ag/AgX (X= Br, Cl) nanocomposite as a highly efficient visible-light plasmonic photocatalyst, *ACS Nano*, 2011, **5**(6), 4529–4536.
26 A. Tomchenko, Structure and gas-sensitive properties of WO3–Bi2O3 mixed thick films, *Sens. Actuators, B*, 2000, **68**(1–3), 48–52.
27 S. R. Kim, M. K. Parvez and M. Chhowalla, UV-reduction of graphene oxide and its application as an interfacial layer to reduce the back-transport reactions in dye-sensitized solar cells, *Chem. Phys. Lett.*, 2009, **483**(1–3), 124–127.
28 G. Moussavi and M. Mahmoudi, Removal of azo and anthraquinone reactive dyes from industrial wastewaters using MgO nanoparticles, *J. Hazard. Mater.*, 2009, **168**(2–3), 806–812.
29 I. V. Mishakov, *et al.*, Nanocrystalline MgO as a dehydrohalogenation catalyst, *J. Catal.*, 2002, **206**(1), 40–48.
30 G. Moussavi and M. Mahmoudi, Degradation and biodegradability improvement of the reactive red 198 azo dye using catalytic ozonation with MgO nanocrystals, *Chem. Eng. J.*, 2009, **152**(1), 1–7.
31 L.-X. Li, *et al.*, Excellent fluoride removal properties of porous hollow MgO microspheres, *New J. Chem.*, 2014, **38**(11), 5445–5452.
32 G. Moussavi and R. Alizadeh, The integration of ozonation catalyzed with MgO nanocrystals and the biodegradation for the removal of phenol from saline wastewater, *Appl. Catal., B*, 2010, **97**(1–2), 160–167.
33 G. Moussavi, A. Yazdanbakhsh and M. Heidarizad, The removal of formaldehyde from concentrated synthetic wastewater using O3/MgO/H2O2 process integrated with the biological treatment, *J. Hazard. Mater.*, 2009, **171**(1–3), 907–913.
34 B. Kakavandi, *et al.*, Enhanced sono-photocatalysis of tetracycline antibiotic using $TiO^2$ decorated on magnetic activated carbon (MAC@ T) coupled with US and UV: a new hybrid system, *Ultrason. Sonochem.*, 2019, **55**, 75–85.
35 F. Hayati, *et al.*, Ultrasound-assisted photocatalytic degradation of sulfadiazine using MgO@ CNT heterojunction composite: effective factors, pathway and biodegradability studies, *Chem. Eng. J.*, 2020, **381**, 122636.
36 S. Yu, *et al.*, Single-crystalline Bi5O7NO3 nanofibers: hydrothermal synthesis, characterization, growth mechanism, and photocatalytic properties, *J. Colloid Interface Sci.*, 2011, **354**(1), 322–330.
37 H. Cheng, *et al.*, In situ ion exchange synthesis of the novel Ag/AgBr/BiOBr hybrid with highly efficient decontamination of pollutants, *Chem. Commun.*, 2011, **47**(25), 7054–7056.
38 Y. Liu, *et al.*, Enhanced photocatalytic degradation of organic pollutants over basic bismuth (III) nitrate/BiVO4 composite, *J. Colloid Interface Sci.*, 2010, **348**(1), 211–215.
39 S. Balachandran and M. Swaminathan, Facile fabrication of heterostructured Bi2O3–ZnO photocatalyst and its enhanced photocatalytic activity, *J. Phys. Chem. C*, 2012, **116**(50), 26306–26312.
40 A. Cabot, *et al.*, Bi2O3 as a selective sensing material for NO detection, *Sens. Actuators, B*, 2004, **99**(1), 74–89.
41 H. Fu, *et al.*, Visible-light-induced degradation of rhodamine B by nanosized Bi2WO6, *J. Phys. Chem. B*, 2005, **109**(47), 22432–22439.
42 Y. Xu and M. A. Schoonen, The absolute energy positions of conduction and valence bands of selected semiconducting minerals, *Am. Mineral.*, 2000, **85**(3–4), 543–556.
43 A. Hameed, *et al.*, Surface phases and photocatalytic activity correlation of Bi2O3/Bi2O4-x nanocomposite, *J. Am. Chem. Soc.*, 2008, **130**(30), 9658–9659.
44 B. Paulchamy, G. Arthi and B. Lignesh, A simple approach to stepwise synthesis of graphene oxide nanomaterial, *J. Nanomed. Nanotechnol.*, 2015, **6**(1), 1.
45 N. Akhtar, *et al.*, Synthesis and characterization of MXene/BiCr2O4 nanocomposite with excellent electrochemical properties, *J. Mater. Res. Technol.*, 2021, **15**, 2007–2015.
46 N. Akhtar, *et al.*, Coprecipitation synthesis and microstructure characterization of nanocomposite $SrCr_2O_4$/MXene, *Mater. Sci. Semicond. Process.*, 2022, **140**, 106407.
47 N. Akhtar, *et al.*, Synthesis and characterization of graphene oxide-based nanocomposite NaCr2O4/GO for electrochemical applications, *J. Mater. Res. Technol.*, 2021, **15**, 6287–6294.
48 R. Shafique, *et al.*, Graphene Oxide/Nickel Chromite Nanocomposite: Optimized Synthesis, Structural and Optical Properties, *ECS J. Solid State Sci. Technol.*, 2021, **10**(10), 101005.

49 R. Shafique, *et al.*, Copper chromite/graphene oxide nanocomposite for capacitive energy storage and electrochemical applications, *Int. J. Environ. Sci. Technol.*, 2022, **19**(8), 7517–7526.
50 R. Shafique, *et al.*, Investigations of 2D $Ti_3C_2$ (MXene)-CoCr2O4 nanocomposite as an efficient electrode material for electrochemical supercapacitors, *Int. J. Energy Res.*, 2022, **46**(5), 6689–6701.
51 T. Yaqoob, *et al.*, MXene/Ag2CrO4 Nanocomposite as Supercapacitors Electrode, *Materials*, 2021, **14**(20), 6008.
52 J. Gupta, *et al.*, Superparamagnetic iron oxide-reduced graphene oxide nanohybrid-a vehicle for targeted drug delivery and hyperthermia treatment of cancer, *J. Magn. Magn. Mater.*, 2018, **448**, 332–338.
53 S. Li, *et al.*, One-step co-precipitation method to construct black phosphorus nanosheets/ZnO nanohybrid for enhanced visible light photocatalytic activity, *Appl. Surf. Sci.*, 2019, **497**, 143682.
54 Z. Wang, *et al.*, Highly photocatalytic ZnO/In2O3 heteronanostructures synthesized by a coprecipitation method, *J. Phys. Chem. C*, 2009, **113**(11), 4612–4617.
55 K. D. Harris, M. Tremayne and B. M. Kariuki, Contemporary advances in the use of powder X-ray diffraction for structure determination, *Angew. Chem., Int. Ed.*, 2001, **40**(9), 1626–1651.
56 B. N. Kumar, *et al.*, Synthesis and characterization of copper particles decorated reduced graphene oxide nano composites for the application of supercapacitors, *AIP Conf. Proc.*, 2018, **1992**(1), 040008.
57 T. Nakajima, A. Mabuchi and R. Hagiwara, A new structure model of graphite oxide, *Carbon*, 1988, **26**(3), 357–361.
58 Y.-D. Ding, *et al.*, Synthesizing MgO with a high specific surface for carbon dioxide adsorption, *RSC Adv.*, 2015, **5**(39), 30929–30935.
59 Y.-C. Wu, *et al.*, Morphology-controllable $Bi_2O_3$ crystals through an aqueous precipitation method and their photocatalytic performance, *Dyes Pigm.*, 2013, **98**(1), 25–30.
60 S. Aksay, Effects of Al dopant on XRD, FT-IR and UV–vis properties of MgO films, *Phys. B*, 2019, **570**, 280–284.
61 R. Schoonheydt and C. Johnston, Surface and interface chemistry of clay minerals, *Dev. Clay Sci.*, 2006, **1**, 87–113.
62 K. Sohlberg, A dual carrier adsorbate-modulated surface conductance model better captures the thermal dependence of conductance $TiO_2$ and $MoO_3$ powders than an inter-grain hopping model, *React. Kinet. Mech. Catal.*, 2020, **131**, 19–35.
63 H. Kamiya, *et al.*, Characteristics and behavior of nanoparticles and its dispersion systems, in *Nanoparticle Technology Handbook*, Elsevier, 2008, pp. 113–176.
64 R. Xu, Progress in nanoparticles characterization: Sizing and zeta potential measurement, *Particuology*, 2008, **6**(2), 112–115.
65 K. Sen and S. Chattoraj, A comprehensive review of glyphosate adsorption with factors influencing mechanism: kinetics, isotherms, thermodynamics study, *Intelligent Environmental Data Monitoring for Pollution Management*, 2021, pp. 93–125.
66 Y.-G. Lu, *et al.*, Preparation and visible light responsive photocatalytic activity of nitrogen-doped Bi (2) O (3) photocatalyst, *J. Inorg. Mater.*, 2012, **26**(6), 643–648.
67 M. M. Rahman, *et al.*, Ultra-sensitive, selective and rapid carcinogenic Bisphenol A contaminant determination using low-dimensional facile binary Mg-SnO2 doped microcube by potential electro-analytical technique for the safety of environment, *J. Ind. Eng. Chem.*, 2022, **109**, 147–154.
68 A. Roy and C. R. Patra, Vanadium pentoxide nanomaterials and their role in anti-angiogenesis for cancer treatment, *Nanomedicine*, 2020, 2643–2646.
69 A. Abd-Elrahim and M. A. Ali, Facile synthesis of nano-sized zinc-rich ZnCdS ternary alloy and UV-irradiation curing of photoluminescence emission characteristics, *Opt. Mater.*, 2021, **122**, 111774.